PAPER

Check for updates

Strong plasmon–exciton coupling in colloidal halide perovskite nanocrystals near a metal film†

C. Meric Guvenc, [ID]ᵃ Nahit Polatᵇ and Sinan Balci [ID] *ᵇ

All inorganic colloidal halide perovskite nanoplatelets and nanowires are highly anisotropic shaped semiconductor nanocrystals with highly tunable optical properties in the visible spectrum. These nanocrystals have large exciton binding energies and high oscillator strengths due to their strongly quantum confined natures. The optical properties of the halide perovskites are tunable by variation of halide composition and morphology of the nanocrystals. We herein demonstrate that colloidal perovskite nanocrystals (NCs) placed in close proximity to chemically functionalized metal films show mixed plasmon–exciton formation, plexciton formation, in the strong coupling regime. The optical properties of all-inorganic lead halide perovskite NCs were controlled by colloidally synthesizing NCs with different morphologies such as nanowires and nanoplatelets or by controlling the composition of the halides in the NCs. The experimentally observed Rabi splitting energies are around 90 meV, 70 meV, and 55 meV for $CsPbI_3$ nanoplatelets, $CsPbI_3$ nanowires, and $CsPb(Br/I)_3$ nanoplatelets, respectively. In addition, the numerical simulations are in good agreement with the experimentally obtained data. The results show that colloidal all-inorganic halide perovskite NCs are promising and strong candidates for studying light–matter interaction at nanoscale dimension.

1. Introduction

The study of light–matter interactions at nanoscale dimension is fundamental and essential for emerging applications in areas such as photovoltaics, biosensors, lasers, and plasmonic circuits.[1–6] Light can be concentrated and tamed at optical frequencies on the nanoscale dimension by using noble metal nanostructures and thin films. Under certain conditions, the incident light can couple with the coherent delocalized electron oscillations on metal nanoparticles or metal thin films, known as surface plasmons, and surface plasmon polaritons (SPPs) are formed. Plasmon polaritons propagate along a metal–dielectric interface and are extremely sensitive to the index variation in the interface, and hence they have found applications in label-free chemical and biological sensing.[7] More importantly, the SPPs generate an evanescent field, which is perpendicular to the metal–dielectric interface at which the SPPs propagate. Furthermore, when organic and inorganic semiconductors having Frenkel and Wannier–Mott excitons, bound electron–hole pairs, respectively, are carefully placed in this evanescent

field, strong coupling between plasmons and excitons may occur. Then, new mixed states called plexcitons are formed, and they can be clearly observed in the polariton dispersion curves as upper and lower polariton branches.[8–16] In fact, the plexciton polaritons show half-plasmonic and half-excitonic properties and they combine the best aspects of two entirely different worlds, namely plasmonics and excitonics. Furthermore, colloidal plexcitonic nanoparticles of different shapes have been synthesized and their optical properties have been investigated by using various spectroscopic techniques.[17] For example, the radiative transitions and relaxation pathways in colloidal plexcitonic nanoparticles have been extensively studied by using two-dimensional electronic spectroscopy.[18] The plexcitonic nanoparticles have enhanced the light-harvesting of chlorophyll molecules strongly coupled to plasmonic nanoparticles.[19] In addition, the plexciton polaritons can be further mixed with SPPs and, a plexcimon polariton, a new optical hybrid mode has been experimentally and theoretically demonstrated.[14]

In the strong coupling regime, there is a coherent and reversible energy exchange between plasmons and excitons.[20] Unlike the weak coupling case, in the strong coupling regime, the energy levels of the excited state are split, *i.e.*, Rabi splitting. Achieving the strong coupling regime depends on several parameters such as exciton linewidth (γ_{ex}), plasmon linewidth (γ_{sp}), and concentration of the quantum emitter, ($n_{exciton}$).[20–22] If these parameters do not satisfy the strong plasmon–exciton coupling, then the coupled system is actually in the weak

ᵃ *Department of Materials Science and Engineering, Izmir Institute of Technology, 35430 Izmir, Turkey*

ᵇ *Department of Photonics, Izmir Institute of Technology, 35430 Izmir, Turkey. E-mail: sinanbalci@iyte.edu.tr*

coupling regime where the system cannot able to produce new hybrid modes, and SPPs and excitons preserve their initial optical modes. In this weakly coupled regime, for example, the spontaneous emission rate of the quantum emitters can be enhanced or suppressed when compared with their free space spontaneous emission form due to the Purcell effect.[23,24] Until now, strong coupling between plasmon and exciton has been observed by using a variety of organic and inorganic semiconducting materials showing Frenkel and Wannier–Mott type excitons, respectively.[25] Although organic semiconducting materials bearing Frenkel type excitons have localized excitonic states with high exciton binding energies and small exciton Bohr radius, inorganic semiconducting materials having Wannier–Mott type excitons have delocalized excitonic states with low exciton binding energies and large exciton Bohr radius.[26] However, quantum size effects provide localization of energy levels, reduce exciton phonon coupling, and increase the exciton binding energy in inorganic colloidal quantum dots.[27] Therefore, owing to the quantum size effects, strong plasmon–exciton coupling at room temperature has been observed in Wannier–Mott excitons coupled to the surface plasmon polariton fields. Recently, various semiconducting materials such as colloidal CdSe quantum dots,[15,16] CdSe nanoplatelets,[28] CdSe@CdS core–shell nanoplatelets,[29] two dimensional transition metal dichalcogenides,[30–32] two dimensional organo-lead halide perovskites,[33–36] J-aggregates,[17] and photochromic dye molecules[37] have been used for the observation of strong plasmon–exciton coupling at room temperature. One of the strong candidates among Wannier–Mott excitons for strong plasmon–exciton coupling is halide perovskite nanocrystals (NCs). Halide perovskites are promising inorganic semiconductor materials due to their unique optical properties such as high defect tolerance, narrow emission peak, high photoluminescence quantum yield, tunability of their optical properties, and high exciton binding energies.[38–45] Also, we note that high exciton binding energies in halide perovskite NCs result in high excitonic effects and high oscillator strength and hence induce strong light–matter interaction for halide perovskite NCs.[46] Symonds et al.[33] observed strong plasmon–exciton coupling in $(C_6H_5C_2H_4-NH_3)PbI_4$ two dimensional layered organo-lead halide perovskites spin coated on a silver surface. They observed around 160 meV of Rabi splitting energy in the Kretschmann configuration. Moreover, Wang et al.[35] observed a very large Rabi splitting energy of 320 meV in two dimensional organo-lead halide perovskites placed in an optical microcavity. However, strong plasmon–exciton coupling in all inorganic halide perovskite NCs placed near a metal thin film or colloidal metal nanoparticles has not been shown yet.

In this study, we investigate coherent energy exchange between SPPs of silver thin film and excitons of colloidal halide perovskite NCs, which have nanoplatelet and nanowire morphology, and several halide ratios. Our experimental and theoretical results show that the dispersion curves obtained from the halide perovskite NCs on metal thin films show upper and lower polariton branches. In other words, the SPPs of the silver film couple with the excitons of the perovskite NCs and thus, in the strong coupling regime,

plasmon–exciton mixed states called perovskite plexcitons are formed. Furthermore, we show that Rabi splitting energy of the coupled system can be tuned by varying the halide composition or morphology of the colloidal halide perovskite NCs.

2. Experimental section

Materials

Lead(II) iodide (PbI_2, 99%), Cesium acetate ($C_2H_3CsO_2$, 99.99%, Sigma-Aldrich), Cesium carbonate (Cs_2CO_3, 99.9%, Sigma-Aldrich), 1-octadecene (ODE, 90%, Sigma-Aldrich), oleylamine (OLAM, 70%) and oleic acid (OA, 90%) were purchased from Sigma-Aldrich. Toluene ($\geq$99%, Merck) was purchased and used without any further purification.

Synthesis of Cs-oleate for nanowires

In a standard synthesis of Cs-oleate, 81.4 mg of Cs_2CO_3, 4 mL of ODE, and 1.25 mL of OA were loaded in a glass tube and dried under vacuum for 1 h at 120 °C. After degassing, the temperature was increased to 150 °C under the flow of nitrogen gas and then Cs-oleate was obtained after 2 h. Before its use in the synthesis of $CsPbI_3$, Cs-oleate solution was heated to 100 °C in order to completely dissolve Cs-oleate in ODE.

Synthesis of Cs-oleate for nanoplatelets

Briefly, 96 mg of cesium acetate was dissolved in 10 mL of OA under ultrasonication until a clear solution was obtained. The final solution was stored in the ambient condition for further use.

$CsPbI_3$ nanoplatelet synthesis

$CsPbI_3$ NPLs were synthesized by using a previously described route by Huang et al.[44] Briefly, 0.1 mmol of PbI_2 powder was completely dissolved in 100 μL of OA, 100 μL of OLAM, and 10 mL of toluene mixture at 80 °C under continuous stirring. Subsequently, 2 mL of PbI_2 precursor solution was added in a glass vial under vigorous stirring at room temperature. Finally, 50 μL of Cs-oleate (for nanoplatelets) solution was quickly injected into the above solution combination and after 2 minutes, the solution was centrifuged at 14 500 rpm for 5 minutes. The obtained precipitate was dispersed in toluene.

$CsPb(Br/I)_3$ nanoplatelet synthesis

$CsPb(Br/I)_3$ NPLs were synthesized by using the same procedure, which was described above. In order to synthesize $CsPb(Br/I)_3$ NPLs, PbI_2 and $PbBr_2$ precursor solution mixtures were used with different amounts for tuning the optical properties of the nanoplatelets. The $PbBr_2$ precursor solution was prepared in a similar to that of PbI_2 precursor solution. During the precursor solution preparation, instead of 0.1 mmol of PbI_2 powder, 0.1 mmol of $PbBr_2$ powder was used.

$CsPbI_3$ nanowire synthesis

$CsPbI_3$ nanowires were synthesized by using a solvothermal process. Firstly, 230.5 mg of PbI_2 was dissolved in 5 mL of ODE, 1 mL of OA and, 1 mL of OLAM mixture at 120 °C under

This journal is © The Royal Society of Chemistry 2020

J. Mater. Chem. C, 2020, **8**, 16520–16526 | **16521**

ambient condition. After the complete dissolution, the obtained solution was cooled down to room temperature. Afterwards, 600 μL of Cs-oleate, which was preheated to 100 °C, was added to the PbI$_2$ precursor solution under continuous stirring. The prepared solution was loaded into the Teflon lined autoclave, and then the autoclave was sealed and placed into the preheated oven at 150 °C for an hour. The nanowire colloid was quenched by immersing in an ice bath and then centrifuged for 10 min at 6000 rpm. The NCs were dispersed in toluene and stored at ambient atmosphere.

Characterization of nanocrystals

Scanning Transmission Electron Microscopy (STEM) analysis of pure and doped samples was carried out in order to observe morphology of the nanocrystals (SEM; Quanta 250, FEI, Hillsboro, OR, USA). The samples were prepared by drop-casting diluted NC suspensions onto 200 mesh carbon-coated copper grids. Absorbance (Abs), Photoluminescence (PL), and time-resolved lifetime (LT) measurements were carried out by using a FS5 Spectrofluorometer (Edinburgh Instruments, UK). Samples were diluted in toluene and the optical properties of the NCs were measured in a cylindrical quartz cuvette. For LT measurements of the samples, the samples were excited with a 450 nm laser with a pulse width of 100 ps and a repetition rate of 1 MHz.

Plasmon–exciton coupling

A well-known Kretschmann configuration was used in order to study strong coupling of perovskite excitons with surface plasmon polaritons (SPPs) of metal thin films.[47] SPPs can be excited by using a prism in the Kretschmann configuration or a metal film coated dielectric diffraction grating.[48] Firstly, a glass substrates were cleaned with a piranha solution, a 3 : 1 mixture of sulfuric acid (95%) and hydrogen peroxide (30%), and then coated with 40 nm thick Ag film fabricated by thermal evaporation of Ag under vacuum. Silver thin films were then inserted into a solution of 10 mL of 10 mM 16-mercaptohexadecanoic acid (90%) in isopropanol for 30 minutes and, subsequently the substrates were washed with isopropanol. Afterwards, the nanocrystals were spin coated on the silver substrates. A tunable laser light source having a spectral width of around 1 nm (Koheras-SuperK Versa) and connected to an acousto-optic tunable filter working in the visible and near infrared region of the electromagnetic spectrum was used in order to obtain dispersion curves of the perovskite NCs on the silver film.

Theoretical calculations

The finite difference time domain (FDTD) method was employed to calculate optical properties of coupled perovskite NCs placed on flat Ag films. In theoretical calculations, the plane wave moves in the z-axis and the mesh size is 1 nm during polariton dispersion curve calculations. The electric field polarization is p-polarized in order to couple incident light to surface plasmons on the flat metal film. A glass prism was used to couple incident light to surface plasmons of metal film. The excitonic modes of the perovskite NCs were assumed to be Lorentzian and expressed as $\varepsilon(\omega) = \varepsilon_\infty + f_0(\omega_0{}^2/(\omega_0{}^2 - \omega^2 - i\gamma_0\omega))$ where the resonance wavelength of the oscillator and the

width of the plasmon resonance (γ_0) were adjusted for each perovskite NCs. The background index was taken as 2.1. The perovskite plexciton dispersion curves were generated by acquiring the reflection spectra for each incidence angle within a broad wavelength range and then the resulting reflectivity distribution for each incidence angle was obtained in a heat map.

3. Results and discussion

Schematic representation of the colloidal perovskite nanocrystals spin coated on a self-assembled monolayers functionalized silver surface is shown in Fig. 1. The silver surface was chemically functionalized with 1-octadecanethiol (ODET) in order to prevent degradation of the silver surface by lead halides. When the metal surfaces are exposed to alkanethiols in a solvent, the thiol containing molecules spontaneously arrange on the metal surface (self-assembled monolayers) by forming very strong metal–thiolate bonds.[49] It should be noted that all-inorganic cesium lead halide based perovskite NCs cause degradation of the silver surface when directly coated on the silver surface. For example, Svanström et al.[50] investigated the degradation of thermally evaporated silver layer on perovskite thin films. They showed that silver thin film cannot be produced continuously without using a barrier layer on the halide perovskite surface. In fact, it was further concluded that the thermally deposited Ag film on the perovskite surface was at the beginning metallic in character but then degraded into AgI or AgBr over time. In our work, we used self-assembled monolayers of ODET molecules as a barrier layer to prevent degradation of the silver surface. It is worth noting that ODET molecules produce alkanethiol self-assembled monolayers on the silver surface due to the strong and spontaneous covalent metal–thiol bond formation. As shown before, alkanethiol layers successfully protect the silver surface from halide ions or environmental effects.[51] Also, in
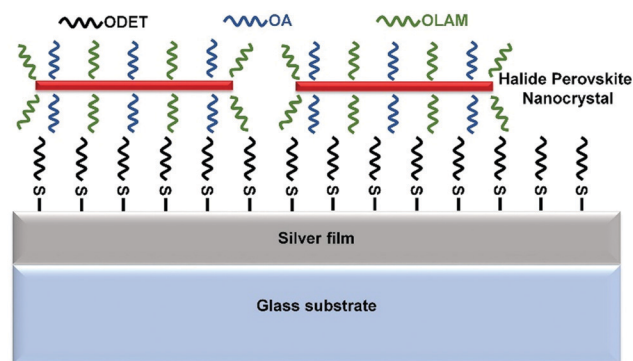

Fig. 1 Schematic drawing of the colloidal halide perovskite NCs placed on a chemically functionalized flat metal film. A 50 nm silver film was thermally evaporated on a glass substrate. The surface of the silver film was uniformly covered with self-assembled monolayers of ODET molecules, which prevent degradation of the silver surface by lead halides. Perovskite NCs in toluene were directly spin-coated on the ODET functionalized silver surface for obtaining perovskite NCs on the metal film. In fact, the OA and OLAM molecules create a ligand shell between the metal film and perovskite NCs. The SPPs of the silver film couple with the excitons of the perovskite NCs and, in the strong coupling regime, perovskite plexcitons are formed.

previous studies, various barrier thin oxide layers (SiO_2, TiO_2, *etc.*) were used to protect silver surfaces from the oxidation or reactive chemicals present in the medium.[52–55] In addition, OA and OLAM molecules used as ligands in the colloidal synthesis of halide perovskite NCs provide additional and significant surface passivation of the NCs.

We now turn our attention to the synthesis and optical properties of halide perovskite NCs used in the observation of perovskite plexcitons on the silver films. Colloidal perovskite NCs exhibit a high photoluminescence quantum yield, very narrow emission and absorption peaks, tunable optical properties, very high exciton binding energies, and strongly quantum confined excitonic states and therefore they are very promising candidates for strong light–matter interaction studies at nanoscale dimension. Fig. 2 shows very narrow emission and absorption spectra of the halide perovskite colloids of $CsPbI_3$ nanoplatelets, $CsPb(Br/I)_3$ nanoplatelets, and $CsPbI_3$ nanowires in toluene. The synthesized NCs have two different band gaps and exciton binding energies.

Indeed, the synthesized perovskite NCs shown in Fig. 2 have very narrow absorption and emission linewidths. More specifically, $CsPbI_3$ nanoplatelets have a narrower PL emission and a bandgap, and a higher exciton binding energy than $CsPb(Br/I)_3$ nanoplatelets due to the increased exciton phonon coupling in mixed halide perovskite quantum dots.[39] Also, Weidman *et al.*[39] reported that the excitonic peak of the mixed halide perovskite nanoplatelets was broader than those of the monohalide perovskite nanoplatelets. Further, the average PL lifetime of $CsPbI_3$ nanoplatelets is longer than the lifetime of $CsPb(Br/I)_3$ nanoplatelets. It is noteworthy that, in the perovskite NCs, a faster emission has been observed in nanocrystals with wider bandgaps.[38] In general, the PL lifetime of the semiconducting quantum dots strongly depends on the size (band gap) of the quantum dots.[56] The STEM images of the nanoplatelets and nanowires are shown in Fig. 2e and f. Moreover, the large area STEM images show that halide perovskite nanoplatelets are homogenously distributed, Fig. S1 (ESI†). However, in the $CsPbI_3$ nanowires, a few nanocubes were also seen in STEM images, see Fig. S2 (ESI†). Further, a very small peak near 700 nm in the PL spectrum of the nanowires implies the existence of nanocubes in the colloid. The average PL lifetimes of the $CsPb(Br/I)_3$ nanoplatelets, $CsPbI_3$ nanoplatelets, and $CsPbI_3$ nanowires are 8.7 ns, 21 ns, and 55.4 ns, respectively. As expected, nanowires have longer PL lifetime than nanoplatelets owing to the narrower bandgap of $CsPbI_3$ nanowires than $CsPbI_3$ and $CsPb(Br/I)_3$ nanoplatelets. Obtained lifetime data of the NCs from the fitted PL lifetime curves were shown in the Table S1 (ESI†).

In the final part, we discuss perovskite plexciton polariton formation in the perovskite NCs deposited on chemically functionalized metal films. The optical properties of the colloidal perovskite NCs were controlled by changing the composition (halide ratio) and the morphology (nanowires and nanoplatelets) of the NCs. The surface plasmons of the silver film was excited by the p-polarized incident light, a tunable laser, in the Kretschmann configuration and hence surface plasmon polaritons are formed. Fig. 3a illustrates the schematic representation of the Kretschmann configuration used for obtaining dispersion curves of the coupled system. The reflection curves from the hybrid nanocrystals-metal thin film samples were taken for each incidence angle in about 0.2 degree intervals. By plotting the reflection intensity in wavelength *versus* the angle of incidence, the optical properties of the metal film were obtained in a heat map, which is the dispersion curve of the SPPs. In fact, strong coupling of the incident light and surface plasmons requires matching of the horizontal
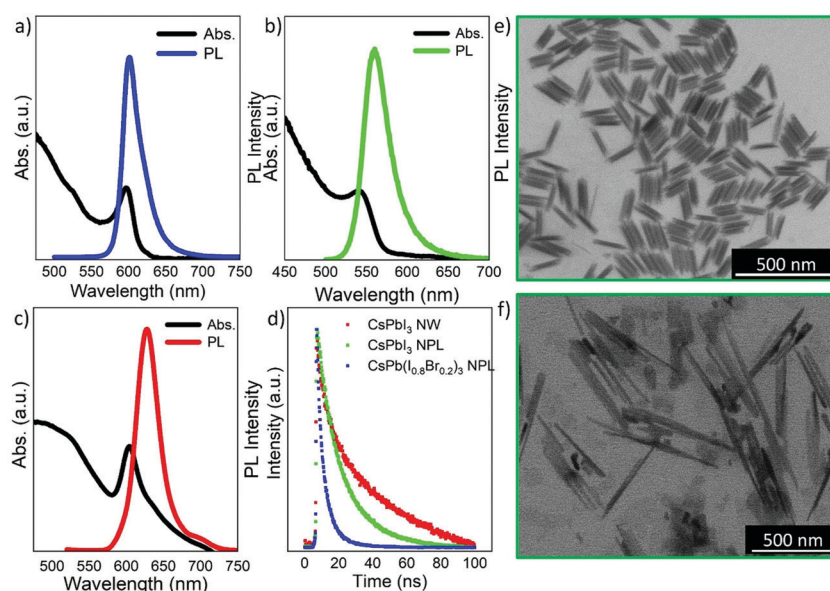
Fig. 2 Optical properties of lead halide perovskite NCs. Emission and absorption spectra of the halide perovskite colloids of (a) $CsPbI_3$ nanoplatelets, (b) $CsPb(Br/I)_3$ nanoplatelets, and (c) $CsPbI_3$ nanowires in toluene show that the synthesized NCs have very narrow absorption and emission linewidths. (d) Time-resolved photoluminescence decays of the colloidal halide perovskite NCs in toluene. The PL measurements were taken at the peak emission wavelength of the NCs. Clearly, the photoluminescence lifetime decreases with increasing quantum confinement in the nanoplatelets, and further decreases with bromine addition in $CsPb(Br/I)_3$ mixed halide nanoplatelets. STEM images of the halide perovskite (e) nanoplatelets, and (f) nanowires.
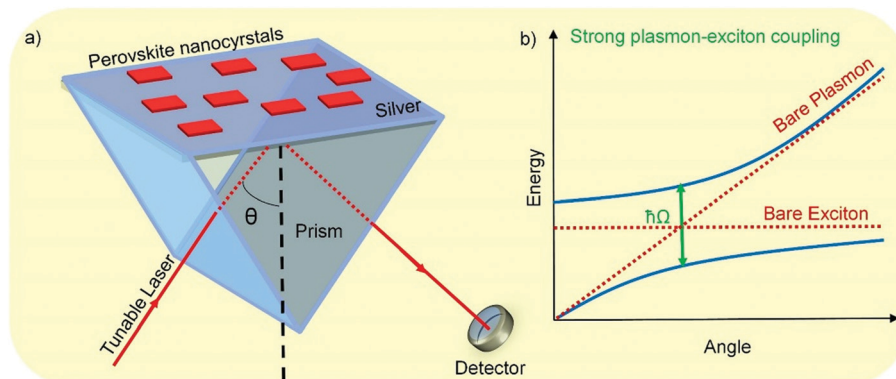
Fig. 3 (a) Schematic representation of the Kretschmann configuration used for obtaining perovskite plexciton dispersion curves. A glass prism increases momentum of the incident light to excite surface plasmons on the flat silver film. Incident light strongly couples with the surface plasmons on the metal film surface and thus surface plasmon polaritons are formed. Lead halide perovskite NCs were placed on chemically modified silver surfaces. Polarization dependent spectroscopic reflection measurements were performed by using a tunable and polarized laser light. The detector collects and measures the intensity of the reflected light from the metal surface. (b) In the strong coupling regime, excitons of the halide perovskite NCs couple with surface plasmon polaritons and thus plasmon–exciton mixed states are formed in the dispersion curves. An anti-crossing behavior observed in the dispersion curve is a clear indication of the strong coupling between excitons of perovskite NCs and SPPs of flat metal film.

component of the incident light momentum, k_x, and real part momentum of the surface plasmons, k_{sp}. Then, the dispersion relation of surface plasmons at the silver film–dielectric interface is $k_x = k_0 n_p \sin(\theta) = k_{sp} = \frac{2\pi}{\lambda}\sqrt{\frac{\varepsilon_m \varepsilon_d}{\varepsilon_m + \varepsilon_d}}$ where k_0 is the free space wavevector of the incident light, n_p is the refractive index of the prism, θ is angle of the incident light, ε_m and ε_d are dielectric constants of the metal and dielectric, respectively, and λ is the wavelength of the incident light.

In the strong coupling regime, SPPs interact with the excitons of perovskite NCs and hence, in the dispersion curve, an anticrossing behavior can be seen, Fig. 3b. The strong interaction of SPPs on the metal surface with optically active materials can be modelled by using a coupled oscillator model as $E_{1,2}(k) = (E_{sp}(k) + E_{ex})/2 \pm 1/2((4g^2 + (E_{sp}(k) - E_{ex})^2))^{1/2}$ where E_1 and E_2 are the upper and lower polariton energies, g is the coupling strength, E_{sp} and E_{ex} are the plasmon and exciton resonance energies, respectively. At the zero detuning, the
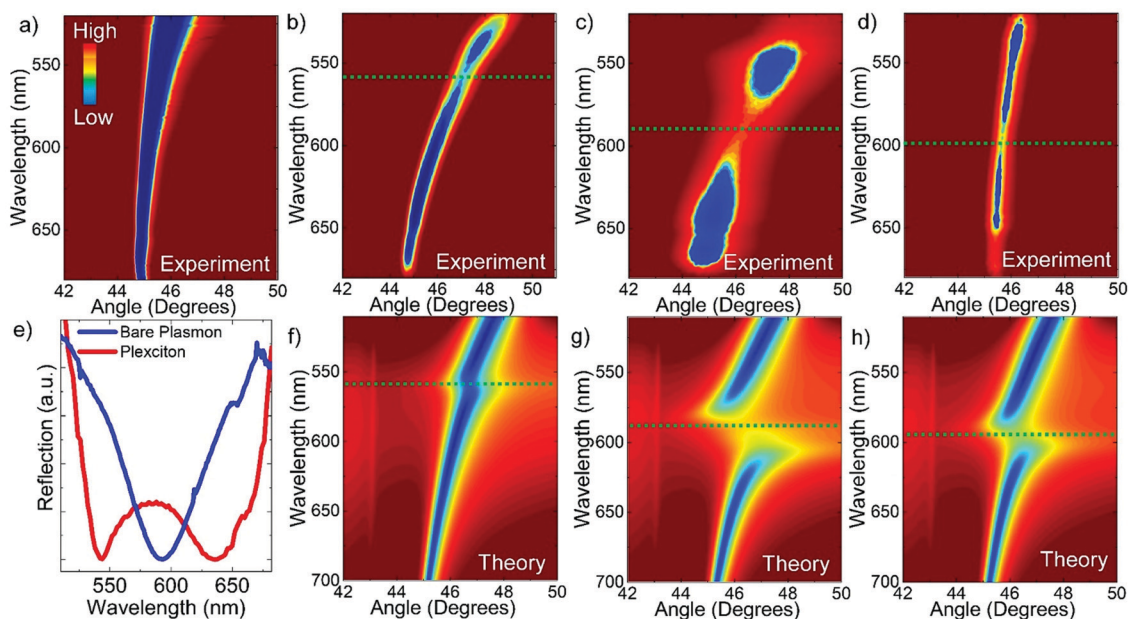
Fig. 4 Experimental and theoretical perovskite plexciton dispersion curves. (a) Dispersion curve of SPPs taken from a bare silver film. Polariton dispersion curves (angle *versus* wavelength) obtained from thin silver films uniformly covered with perovskite NCs; (b) CsPb(Br/I)$_3$ nanoplatelets, (c) CsPbI$_3$ nanoplatelets, and (d) CsPbI$_3$ nanowires. The dotted lines in the dispersion curves show the energy position of the uncoupled perovskite nanocrystal excitons. (e) Reflection curves from a bare silver film having SPP resonance wavelength at around 45.5 degrees and a silver film coated with CsPbI$_3$ nanoplatelets at around 46 degrees. The upper and lower polariton branches in the reflection curve are visible. Theoretically obtained polariton dispersion curves from a silver film coated with (f) CsPb(Br/I)$_3$ nanoplatelets, (g) CsPbI$_3$ nanoplatelets, and (h) CsPbI$_3$ nanowires.

separation between the upper and lower polariton branches gives the magnitude of the Rabi splitting energy, $\Delta E = E_2 - E_1 = \hbar\Omega = 2g$. In fact, the strong coupling occurs when the coherent energy exchange between plasmons and excitons is greater than their decay rates, $g > (\gamma_{sp} - \gamma_{ex})/2$. However, if $g \le (\gamma_{sp} - \gamma_{ex})/2$, then the interaction is in the weak coupling regime where the irreversible spontaneous emission is, in some cases, suppressed or, in other cases, enhanced.[22,57] SPP dispersion curve obtained from a bare silver film was shown in Fig. 4a. The SPP resonance wavelength can be flexibly controlled by only changing the incidence angle of the laser light. The polariton dispersion curves for the coupled perovskite NCs are shown in Fig. 4b–d for $CsPb(Br/I)_3$ nanoplatelets, $CsPbI_3$ nanoplatelets, and $CsPbI_3$ nanowires, respectively. The largest Rabi splitting energy was observed in the monohalide $CsPbI_3$ perovskite nanoplatelets. This is due to the fact that the monohalide perovskite nanocrystals have lower exciton phonon coupling than the mixed halide perovskite nanocrystals.[39] Furthermore, the Rabi splitting energy decreased significantly with increasing dimensionality and quantum size effects from nanoplatelet to nanowire. Also, note that decreased quantum confinement effect of $CsPbI_3$ nanowires can be detected in the redshifted absorption peak in Fig. 2c. Calculated Rabi splitting energies from the plexciton polariton dispersion curves for $CsPbI_3$ nanoplatelets, $CsPbI_3$ nanowires, and $CsPb(Br/I)_3$ nanoplatelets are ~ 90 meV, ~ 70 meV, and ~ 55 meV, respectively.

4. Conclusions

In conclusion, we experimentally and theoretically demonstrate all-inorganic lead halide perovskite NCs based plexciton formation in the strong coupling regime. The optical properties of all-inorganic lead halide perovskite NCs were controlled by colloidally synthesizing nanocrystals with different morphologies such as nanowires, and nanoplatelets or by controlling the composition of the halides in the perovskite NCs. Colloidal perovskite NCs were placed in close proximity to chemically functionalized metal films. In the strong coupling regime, polariton dispersion curves indicate mixed plasmon–exciton states. In our experiments, the maximum Rabi splitting energy was observed between $CsPbI_3$ nanoplatelets and silver film. In addition, the observed Rabi splitting energy was decreased with increasing dimensionality or mixing halide composition in all-inorganic halide perovskite NCs. The results have shown that all-inorganic halide perovskite NCs exhibit facile synthesis, bright luminescence, tunable and very narrow absorption and emission bands, and strongly quantum confined excitonic states, and hence they are very promising and strong candidates for studying plasmon–exciton interaction. Therefore, perovskite NCs based plexcitons will enable understanding light–matter interaction at nanoscale dimension and find applications in polariton lasers, light emitting diodes, and surface enhanced spectroscopies.

Conflicts of interest

There are no conflicts to declare.

Acknowledgements

References

1   W. L. Barnes, A. Dereux and T. W. Ebbesen, *Nature*, 2003, **424**, 824–830.
2   R. A. Pala, J. White, E. Barnard, J. Liu and M. L. Brongersma, *Adv. Mater.*, 2009, **21**, 3504–3509.
3   E. Ozbay, *Science*, 2006, **311**, 189–193.
4   T. W. Odom and G. C. Schatz, *Chem. Rev.*, 2011, **111**, 3667–3668.
5   S. Christopoulos, G. B. H. von Högersthal, A. J. D. Grundy, P. G. Lagoudakis, A. V. Kavokin, J. J. Baumberg, G. Christmann, R. Butté, E. Feltin, J. F. Carlin and N. Grandjean, *Phys. Rev. Lett.*, 2007, **98**, 126405.
6   H. Yokoyama, *Science*, 1992, **256**, 66–70.
7   R. Ameling and H. Giessen, *Nano Lett.*, 2010, **10**, 4394–4398.
8   N. T. Fofang, T.-H. Park, O. Neumann, N. A. Mirin, P. Nordlander and N. J. Halas, *Nano Lett.*, 2008, **8**, 3481–3487.
9   S. Balci, *Opt. Lett.*, 2013, **38**, 4498–4501.
10 D. E. Westmoreland, K. P. McClelland, K. A. Perez, J. C. Schwabacher, Z. Zhang and E. A. Weiss, *J. Chem. Phys.*, 2019, **151**, 210901.
11 O. Bitton, S. N. Gupta and G. Haran, *Nanophotonics*, 2019, **8**, 559–575.
12 P. Vasa and C. Lienau, *ACS Photonics*, 2017, **5**, 2–23.
13 D. G. Lidzey, D. D. Bradley, A. Armitage, S. Walker and M. S. Skolnick, *Science*, 2000, **288**, 1620–1623.
14 S. Balci and C. Kocabas, *Opt. Lett.*, 2015, **40**, 3424–3427.
15 D. E. Gómez, S. S. Lo, T. J. Davis and G. V. Hartland, *J. Phys. Chem. B*, 2012, **117**, 4340–4346.
16 D. E. Gómez, K. C. Vernon, P. Mulvaney and T. J. Davis, *Nano Lett.*, 2010, **10**, 274–278.
17 S. Balci, B. Kucukoz, O. Balci, A. Karatay, C. Kocabas and G. Yaglioglu, *ACS Photonics*, 2016, **3**, 2010–2016.
18 D. Finkelstein-Shapiro, P.-A. Mante, S. Sarisozen, L. Wittenbecher, I. Minda, S. Balci, T. Pullerits and D. Zigmantas, 2020, arXiv:2002.05642.
19 F. Nan, S. J. Ding, L. Ma, Z. Q. Cheng, Y. T. Zhong, Y. F. Zhang, Y. H. Qiu, X. G. Li, L. Zhou and Q. Q. Wang, *Nanoscale*, 2016, **8**, 15071–15078.
20 S. Balci, C. Kocabas, S. Ates, E. Karademir, O. Salihoglu and A. Aydinli, *Phys. Rev. B: Condens. Matter Mater. Phys.*, 2012, **86**, 235402.
21 C. M. Guvenc, F. M. Balci, S. Sarisozen, N. Polat and S. Balci, *J. Phys. Chem. C*, 2020, **124**, 8334–8340.
22 P. Törmä and W. L. Barnes, *Rep. Prog. Phys.*, 2014, **78**, 013901.
23 E. M. Purcell, H. C. Torrey and R. V. Pound, *Phys. Rev.*, 1946, **69**, 37–38.
24 J. P. Reithmaier, G. Sęk, A. Löffler, C. Hofmann, S. Kuhn, S. Reitzenstein, L. Keldysh, V. Kulakovskii, T. Reinecke and A. Forchel, *Nature*, 2004, **432**, 197–200.
25 J. Frenkel, *Phys. Rev.*, 1931, **37**, 17–44.

26 W. Liang, *Phys. Educ.*, 1970, **5**, 226.

27 J. C. Maan, G. Belle, A. Fasolino, M. Altarelli and K. Ploog, *Phys. Rev. B: Condens. Matter Mater. Phys.*, 1984, **30**, 2253–2256.

28 J. M. Winkler, F. T. Rabouw, A. A. Rossinelli, S. V. Jayanti, K. M. McPeak, D. K. Kim, B. le Feber, F. Prins and D. J. Norris, *Nano Lett.*, 2018, **19**, 108–115.

29 I. Shlesinger, H. Monin, J. Moreau, J.-P. Hugonin, M. Dufour, S. Ithurria, B. Vest and J.-J. Greffet, *ACS Photonics*, 2019, **6**, 2643–2648.

30 F. Deng, H. Liu, L. Xu, S. Lan and A. E. Miroshnichenko, *Laser Photonics Rev.*, 2020, **14**, 1900420, DOI: 10.1002/lpor.201900420.

31 A. H. Rose, J. R. Dunklin, H. Zhang, J. M. Merlo and J. van de Lagemaat, *ACS Photonics*, 2020, **7**, 1129–1134.

32 M. Geisler, X. Cui, J. Wang, T. Rindzevicius, L. Gammelgaard, B. S. Jessen, P. A. D. Gonçalves, F. Todisco, P. Bøggild, A. Boisen, M. Wubs, N. A. Mortensen, S. Xiao and N. Stenger, *ACS Photonics*, 2019, **6**, 994–1001.

33 C. Symonds, J. Bellessa, J. C. Plenet, A. Bréhier, R. Parashkov, J. S. Lauret and E. Deleporte, *Appl. Phys. Lett.*, 2007, **90**, 091107.

34 C. Symonds, C. Bonnand, J. C. Plenet, A. Bréhier, R. Parashkov, J. S. Lauret, E. Deleporte and J. Bellessa, *New J. Phys.*, 2008, **10**, 065017.

35 S. Wang, A. Mika, J. A. Hutchison, C. Genet, A. Jouaiti, M. W. Hosseini and T. W. Ebbesen, *Nanoscale*, 2014, **6**, 7243–7248.

36 Q. Shang, S. Zhang, Z. Liu, J. Chen, P. Yang, C. Li, W. Li, Y. Zhang, Q. Xiong, X. Liu and Q. Zhang, *Nano Lett.*, 2018, **18**, 3335–3343.

37 T. Schwartz, J. A. Hutchison, C. Genet and T. W. Ebbesen, *Phys. Rev. Lett.*, 2011, **106**, 196405.

38 L. Protesescu, S. Yakunin, M. I. Bodnarchuk, F. Krieg, R. Caputo, C. H. Hendon, R. X. Yang, A. Walsh and M. V. Kovalenko, *Nano Lett.*, 2015, **15**, 3692–3696.

39 M. C. Weidman, M. Seitz, S. D. Stranks and W. A. Tisdale, *ACS Nano*, 2016, **10**, 7830–7839.

40 C. M. Guvenc, Y. Yalcinkaya, S. Ozen, H. Sahin and M. M. Demir, *J. Phys. Chem. C*, 2019, **123**, 24865–24872.

41 J.-P. Ma, J.-K. Chen, J. Yin, B.-B. Zhang, Q. Zhao, Y. Kuroiwa, C. Moriyoshi, L. Hu, O. M. Bakr and O. F. Mohammed, *ACS Mater. Lett.*, 2020, **2**, 367–375.

42 G. H. Ahmed, J. Yin, O. M. Bakr and O. F. Mohammed, *J. Chem. Phys.*, 2020, **152**, 020902.

43 Q. A. Akkerman, S. G. Motti, A. R. Srimath Kandada, E. Mosconi, V. D'Innocenzo, G. Bertoni, S. Marras, B. A. Kamino, L. Miranda, F. De Angelis, A. Petrozza, M. Prato and L. Manna, *J. Am. Chem. Soc.*, 2016, **138**, 1010–1016.

44 H. Huang, Y. Li, Y. Tong, E. P. Yao, M. W. Feil, A. F. Richter, M. Döblinger, A. L. Rogach, J. Feldmann and L. Polavarapu, *Angew. Chem., Int. Ed.*, 2019, **58**, 16558–16562.

45 Q. A. Akkerman and L. Manna, *ACS Energy Lett.*, 2020, **5**, 604–610.

46 J. Li, L. H. Luo, H. W. Huang, C. Ma, Z. Z. Ye, J. Zeng and H. P. He, *J. Phys. Chem. Lett.*, 2017, **8**, 1161–1168.

47 S. Balci, E. Karademir and C. Kocabas, *Opt. Lett.*, 2015, **40**, 3177–3180.

48 I. Pockrand, A. Brillante and D. Mobius, *J. Chem. Phys.*, 1982, **77**, 6289–6295.

49 L. Kankate, A. Turchanin and A. Golzhauser, *Langmuir*, 2009, **25**, 10435–10438.

50 S. Svanström, T. J. Jacobsson, G. Boschloo, E. M. J. Johansson, H. Rensmo and U. B. Cappel, *ACS Appl. Mater. Interfaces*, 2020, **12**, 7212–7221.

51 C. Liang, C. Yang and N. Huang, *Surf. Coat. Technol.*, 2009, **203**, 1034–1044.

52 Y. J. Xu, J. X. Liao, Q. W. Cai and X. X. Yang, *Sol. Energy Mater. Sol. Cells*, 2013, **113**, 7–12.

53 Y. J. Xu, Q. W. Cai, X. X. Yang, Y. Z. Zuo, H. Song, Z. M. Liu and Y. P. Hang, *Sol. Energy Mater. Sol. Cells*, 2012, **107**, 316–321.

54 A. Dagamseh, B. Vet, F. Tichelaar, P. Sutta and M. Zeman, *Thin Solid Films*, 2008, **516**, 7844–7850.

55 C. Kennedy, R. Smilgys, D. Kirkpatrick and J. Ross, *Thin Solid Films*, 1997, **304**, 303–309.

56 I. Lignos, R. M. Maceiczyk, M. V. Kovalenko and S. Stavrakis, *Chem. Mater.*, 2020, **32**, 27–37.

57 J. Dintinger, S. Klein, F. Bustos, W. L. Barnes and T. W. Ebbesen, *Phys. Rev. B: Condens. Matter Mater. Phys.*, 2005, **71**, 035424.